Lawrence Berkeley National Laboratory

Title
Role of Hydrogen in Defining the n-Type Character of BiVO4 Photoanodes

Authors
Cooper, Jason K
Scott, Soren B
Ling, Yichuan
et al.

The Role of Hydrogen in Defining the n-Type Character of BiVO4 Photoanodes

SCHOLARONE™
Manuscripts

The Role of Hydrogen in Defining the n-Type Character of BiVO$_4$ Photoanodes

Jason K. Cooper,[a,b] Soren B. Scott,[a] Yichuan Ling,[c] Jinhui Yang,[a,b] Sijie Hao,[d] Yat Li,[c] Francesca M. Toma,[a,b] Martin Stutzmann,[d] K. V. Lakshmi,[e] and Ian D. Sharp[a,b,*]

[a.] Joint Center for Artificial Photosynthesis, Lawrence Berkeley National Laboratory, Berkeley, CA 94720, United States

[b.] Chemical Sciences Division, Lawrence Berkeley National Laboratory, Berkeley, CA 94720, United States

[c.] Department of Chemistry and Biochemistry, University of California, Santa Cruz, CA 95064, United States

[d.] Walter Schottky Institut and Physik Department, Technische Universität München, Am Coulombwall 4, 85748 Garching, Germany

[e.] Department of Chemistry and Chemical Biology and The Baruch '60 Center for Biochemical Solar Energy Research, Rensselaer Polytechnic Institute, Troy, NY 12180, United States

ABSTRACT: The roles of hydrogen impurity and oxygen vacancy defects on defining the conductivity, and hence photoelectrochemical (PEC) performance characteristics, of monoclinic scheelite bismuth vanadate (BiVO$_4$) are investigated using a combination of experiment and theory. We find that elemental hydrogen is present as an impurity in as-synthesized BiVO$_4$ and that increasing its concentration by annealing in H$_2$ at temperatures up to 290 °C leads to near-complete elimination of majority carrier transport limitations, a beneficial shift in the photoanodic current onset potential, and improved fill factor. Magnetic resonance measurements reveal that hydrogen can be incorporated in at least two different chemical environments, which are assigned to interstitial and substitutional sites. Incorporation of hydrogen leads to a shift of the Fermi level towards the conduction band edge, indicating that n-type character is correlated with increased hydrogen content. This finding is in agreement with theory and reveals that hydrogen acts as a donor in BiVO$_4$. Sub-bandgap photoluminescence is observed from as-synthesized material and is consistent with deep electronic states associated with oxygen vacancies. Hydrogen treatment leads to reduced emission from these states. These findings support the conclusion that hydrogen, rather than oxygen vacancies, is dominant in determining the n-type conductivity of BiVO$_4$. These findings have important implications for controlling the electronic properties and functional characteristics of this promising photoanode material.

■ INTRODUCTION

Photoelectrochemical (PEC) water splitting is a promising route to capture and store solar energy as hydrogen in a single step.[1,2] One advantage to this approach is the natural charge-separating ability of semiconductor-liquid junctions, which can provide large photovoltages, even over complex surface topography, without need for forming solid-state semiconductor junctions.[2-4] Among photoelectrode materials, thin film transition metal oxide semiconductors have attracted considerable interest due to their potential for low cost, ease of fabrication, and improved stability relative to the semiconductors more commonly used in the photovoltaics industry. However, these oxide materials are often characterized by deviations from ideal stoichiometry and complex defect properties. Improved understanding and control of the mechanisms of charge separation, transport, and recombination, which are largely defined by crystal defects and impurities, is important for advancing progress within this class of materials.

Bismuth vanadate (BiVO$_4$) is one of the most actively investigated oxide semiconductors for PEC energy conversion due to its moderate indirect bandgap of 2.5 eV,[5] favourable conduction band position,[6] and relatively long photocarrier lifetimes.[6-8] However, poor majority carrier transport, arising from formation of electron small polarons, has been identified as one of the primary limitations on its PEC performance.[9-12]

To overcome this issue, the best-performing BiVO$_4$ films incorporate n-type dopants, such as tungsten or molybdenum, to increase n-type conductivity,[13] nanostructured architectures to decrease transport lengths while increasing semiconductor/electrolyte junction areas,[14-16] or carrier selective contacts to reduce photocarrier recombination rates.[17] While these advances have yielded impressive performance improvements, basic understanding and control of defect properties in this material remain lacking. This is exemplified by the discrepancy between calculations of intrinsic defect formation energies and experimentally obtained conductivities in synthesized thin films. In particular, density functional theory (DFT) calculations by Yin *et al.* predict that BiVO$_4$ should have p-type character when synthesized under O-rich conditions and n-type character when synthesized under O-poor/Bi-rich conditions.[18] In contrast, experimentally synthesized films, which are typically annealed at high temperature for long times in oxygen or air (i.e. under O-rich conditions), consistently exhibit n-type conductivity. While this native n-type conductivity is typically attributed to the presence of oxygen vacancies (O$_{vac}$), which act as shallow donors in BiVO$_4$, these synthesis conditions should favour dominant formation of bismuth vacancies (Bi$_{vac}$), which are shallow acceptors. Equilibrium between these two lowest formation energy defects under O-rich conditions should result in a Fermi level that is pinned approximately 0.55 eV above the valence band maximum (VBM). The strik-

ing difference between theory and experiment provides a clue that unidentified and uncontrolled impurity defects may play a defining role in determining the conductivities, and thus functional characteristics, of $BiVO_4$ photoanodes.

Hydrogen is known to be ubiquitous in synthesis and processing environments, readily diffuses, and is difficult to detect experimentally.[19] However, it has also been shown to play a significant role in affecting the electronic properties of a range of semiconductors. For example, the recognition that interstitial and oxygen site substitutional hydrogen (H_{int} and H_O, respectively) act as shallow donors in ZnO[20,21] was important for resolving many previously poorly understood and apparently contradictory experimental observations. For the case of $BiVO_4$, annealing in hydrogen has been shown to improve its PEC performance by increasing its n-type conductivity.[22-24] However, the mechanisms by which H_2 annealing does this are not yet clear and the role of residual hydrogen during synthesis has not been addressed.

In the present work, we explore the role of hydrogen in defining the electronic properties of $BiVO_4$. We find that annealing of $BiVO_4$ films in H_2 at moderate temperature increases PEC performance by increasing the n-type character of the material and reducing mid-gap electronic states. Application of the hydrogen treatment to advanced nanoporous $BiVO_4$ films reveals that majority carrier transport limitations can be almost entirely eliminated, thereby enabling front-illuminated configurations with this high performance material. Although it is often assumed that formation of oxygen vacancy defects, which act as electron donors, is the dominant effect of annealing metal oxide semiconductors in hydrogen, we find that hydrogen in $BiVO_4$ plays an active role in defining its n-type conductivity. In particular, magnetic resonance measurements confirm that hydrogen incorporates into $BiVO_4$ and photoluminescence spectroscopy, combined with first principles calculations, indicates reduced radiative recombination at deep electronic states, which are consistent with those introduced by oxygen vacancies. These findings, together with recent breakthroughs in understanding polaron transport in $BiVO_4$,[9-12] point to important roles for interactions between polarons and lattice defects on defining majority carrier mobility. Finally, we also find that residual hydrogen in as-synthesized $BiVO_4$ films may have a direct impact on conductivity and electronic transport properties. Thus, consideration and control of the annealing atmosphere and precursors during synthesis, which are commonly overlooked in formation of metal oxide semiconductors, is important for defining functional PEC characteristics.

■ EXPERIMENTAL SECTION

BiVO₄ Thin Film Synthesis and Processing
Spin-coated bismuth vanadate thin films were prepared by adapting a literature procedure.[25,26] In a typical deposition, 15 mL of a 0.2 M solution of bismuth (III) nitrate pentahydrate (Sigma Aldrich, ≥98%) in acetylacetone (Sigma Aldrich, ≥99%) and 100 mL of a 0.03 M solution of vanadium(IV)-oxy acetylacetonate in acetylacetone were prepared separately, and sonicated for 10 min. Next, the two solutions were mixed together and sonicated for an additional 5 min. Approximately 1-1.2 mL of this resulting solution – enough to homogeneously cover the substrate surface – was filtered with a 0.45 µm nylon filter (Thermo Scientific) and dispensed onto a 100 mm wafer of fused silica (4 W 55, Hoya Corporation USA, Milpitas, CA) for optical measurements or plates of fluorine-doped tin oxide (FTO) on glass for photoelectrochemical measurements (Sigma-Aldrich, 100 mm x 100 mm x 2 mm, TEC 15, ~13 Ω □⁻¹). Prior to deposi-

tion, substrates were thoroughly washed with isopropanol and with detergent and deionized water, dried with a nitrogen gun, and treated for 10 min in an ozone cleaner (Jelight Model 42). The substrate, with precursor solution covering its surface, was then spun twice in a row at 1000 rpm for 6 s on a Laurell Technologies spin coater with an acceleration rate of 150 rpm/s. After this spin-coating cycle, the substrate was annealed for 10 min at 500 °C in a muffle furnace. This procedure (i.e. spin-coating followed by short annealing) was repeated nine times. After the final spin-coating cycle, the substrate was annealed for 2 h at 500 °C to achieve a final thickness of ~50 nm.

BiVO₄ Powder Synthesis
Monoclinic scheelite $BiVO_4$ powder was synthesized by solid-solid reaction between Bi_2O_3 and V_2O_5. 7.193 g of Bi_2O_3 (99.99%, Sigma Aldrich) and 2.808 g of V_2O_5 (99.95%, Sigma Aldrich) were mixed, giving a 1:1 stoichiometric ratio of bismuth to vanadium. The powders were ground together with a mortar and pestle, dispersed in ethanol to increase the homogeneity of the mixture, dried overnight, pressed into a pellet, and heated in a furnace at 600 °C in air for 72 h. After cooling, the pellet was crushed into a bright yellow powder. XRD showed a small amount of unreacted V_2O_5, so the powder was again ground with a mortar and pestle, pressed into a pellet and placed in the furnace for an additional 48 h at 650 °C. After the second round of heating, XRD confirmed that the product powder consisted of pure monoclinic scheelite $BiVO_4$, with unreacted V_2O_5 below the detection limit (Figure S3). Some of the powder was post-treated in H_2, as described for thin films.

Electrodeposited BiVO₄ Thin Film Synthesis and Processing
Electrodeposited $BiVO_4$ films were prepared on FTO glass substrates using a previously published protocol by Kim *et al.*, with slight modifications.[16] Briefly, 0.04 M $Bi(NO_3)_3 \cdot 5H_2O$ was dissolved in acidified (pH 1.7, HNO_3) 0.4 M KI. Separately, 0.23 M *p*-benzoquinone was dissolved in 200 proof ethanol (ACS reagent grade, Sigma-Aldrich). Prior to deposition, 50 mL of the $Bi(NO_3)_3$ solution was mixed with 20 mL of the *p*-benzoquinone. FTO/glass electrodes were cleaned with detergent and deionized water, cut into 1.5×1.5 cm² squares, cleaned by sonication for 15 min in 1:1 acetone:isopropyl alcohol, and dried under N_2. Contact was made with copper tape. The electrode area was 1×1 cm² area using electroplating tape 470 (3M) to shield the other areas of the electrode and the copper tape. BiOI was electrochemically deposited from the above mixture onto the FTO electrodes in a 3 electrode cell with Pt mesh counter electrode and 3 M Ag/AgCl reference electrode at a potential of -0.1 V vs. Ag/AgCl for 5 min. After rinsing and drying with N_2, 200 µL of 0.2 M $VO(acac)_2$ in DMSO was deposited on the BiOI layer and annealed in a muffle furnace at atmospheric conditions for 2 h at 450 °C. After annealing, the electrodes were immersed in 0.1 M NaOH to remove remaining V_2O_5. Scanning electron microscopy was used to compare the morphologies of spin coated and electrodeposited films, as shown in Fig. S1. As expected, the electrodeposited material was characterized by a nanoporous morphology. Subsequently, these samples were split in half, with one half treated by H_2 annealing and the other half retained as a control.

H₂ Annealing
Samples of $BiVO_4$ were annealed in a quartz glass tube furnace equipped with a vacuum pump and mass flow controllers for flowing N_2 and H_2 gasses. The quartz tube was conditioned prior to annealing samples by a 550 °C air anneal for 2 h followed by a N_2 anneal at 200 °C for 1 h and, finally, a H_2 anneal at 350 °C for 1 h. Samples were annealed in 1 atm of H_2. The procedure for charging the quartz reactor included 3× evacuations to at least 200 mTorr, with a N_2 purge between each pump cycle, with a final pumping step to at least 100 mTorr. The tube was then filled with H_2. The flow rate of H_2 was kept constant at 150 sccm for the duration of the annealing treatment. The heating rate was 1 °C/s and the annealing time was 15 min at the target temperature, after which the clam shell of the furnace was opened and allowed to cool to room temperature. Once cooled, the flow was switched from H_2 to N_2 and the tube was purged for ~5 min prior to removing the sample.

Photoelectrochemical Characterization
Photoelectrochemical (PEC) testing was performed with a Biologic SP-300 potentiostat using a three electrode configuration with a Pt counter electrode and 3M Ag/AgCl reference electrode at a scan rate of 50 mV s⁻¹. All PEC measurements presented here were performed in the presence of sodium sulfite as a sacrificial hole acceptor. The use of sulfite, which is characterized by facile oxidation kinetics, allows for evaluation of differences in PEC performance due to photon absorption and photocarrier transport within the semiconductor, without influence from changes of the

2

native catalytic activity of the surface.[27] For spin-coated films, the electrolyte was 1 M phosphate buffer (1:1 K_2HPO_4 and KH_2PO_4) at pH 6.8 with 0.1 M Na_2SO_3 as a sacrificial hole acceptor. For nanoporous $BiVO_4$ films, the electrolyte was 0.5 M phosphate butter (1:1 K_2HPO_4 and KH_2PO_4) with 1 M Na_2SO_3 as a sacrificial hole acceptor at pH 7.16. In this case, the higher concentration of hole acceptor was used for comparison with literature results.[16] Simulated AM 1.5G solar illumination was provided by a Solar Light solar simulator (16S-300-002 V4.0 Air Mass 1.5 simulator) with a flux of 100 mW cm^{-2}, as determined by a calibrated Newport Si PV module.

According to common practice, we use as a figure of merit the photocurrent density at 1.23 V vs. RHE, which is arbitrary with respect to sulfite oxidation but provides a useful indication of the saturation current density (J_{SC}) before the onset of dark current. We note that Mott-Schottky analysis for determination of donor densities and flatband potentials yielded non-idealities that precluded quantification. Therefore, as a second figure of merit, we use the onset potential (E_{onset}), herein defined as the potential at which the anodic photocurrent reaches 1 μA cm^{-2} in the anodic sweep of the second cycle of a cyclic voltammogram.

Materials Characterization

X-ray photoelectron spectroscopy (XPS) was performed using a monochromatized Al Kα source (hν = 1486.6 eV), operated at 150 W, on a Kratos Axis Ultra DLD system at a take-off angle of 0° relative to the surface normal, and pass energy for narrow scan core level and valence band spectra of 20 eV. Spectral fitting was performed using Casa XPS analysis software. Spectral positions were corrected using adventitious carbon by shifting the C 1s core level position to 284.8 eV and curves were fit with quasi-Voigt lines following Shirley background subtraction.

The ^1H magic angle spinning (MAS) solid-state nuclear magnetic resonance (NMR) spectroscopy measurements were performed on a Bruker Avance I 500 MHz NMR spectrometer equipped with a 4 mm H/X magic angle spinning probe with a resonance frequency of 500.23 MHz. The ^1H spectra were acquired with a 90° pulse of 5.25 μs duration, relaxation delay of 1 s, and 13 kHz spinning speed.

Raman spectroscopy was performed with a Horiba Jobin Yvon LabRAM HR confocal Raman microscope with 633 nm excitation.

The electron paramagnetic resonance (EPR) spectra were obtained on a Bruker Elexsys 580 EPR spectrometer. The variable-temperature cw EPR measurements were performed with a super high-Q (SHQE) resonator (ER 4123SHQE) (Bruker BioSpin, Billerica, MA, USA) that was equipped with a continuous-flow helium E900 cryostat (Oxford Instruments, Oxfordshire, U.K.) employing liquid helium for temperatures between 4-10 K. The operating frequency of the ER 4123SHQE resonator was 9.386 GHz and all of the spectra were acquired at 4 K with a modulation frequency of 100 kHz and modulation amplitude of 2 G. The V_2O_5 and $BiVO_4$ powders and films were loaded into 4 mm quartz EPR tubes (Wilmad Labglass, Vineland, NJ, USA) and rapidly frozen at 77 K.

Photoluminescence measurements were performed on a custom-built instrument. Temperature control was achieved using a 10 K closed cycle He cryostat (Janus Research Company, Wilmington, MA, USA) equipped with a temperature controller (Model 335, Lake Shore Cryotronics, Inc., Westerville, OH, USA). The sample was excited with a 405 nm continuous wave laser (100 mW Excelsior, Spectra-Physics, Santa Clara, CA, USA) after passing the beam through a 405 nm notch filter and attenuating to 3 mW with a spot size of 2 mm. The photoluminescence from the sample was collected through a 407 nm long pass filter and focused onto the inlet slit of an Andor Shamrock spectrometer equipped with a 600 lines/mm grating blazed at 500 nm (Andor Technology Ltd., Belfast, UK). The spectra were recorded with an Andor iDus 410 CCD detector operated at -90 °C. Wavelength calibration was performed with a Hg calibration lamp and correction for the spectral response of the setup was achieved using a 45 W NIST-traceable quartz tungsten halogen light source with known colour temperature.

Room temperature absorption was measured by transverse photothermal deflection spectroscopy (PDS) according to Ref. [28] and references therein.[28] The sample was located in a quartz cuvette filled with C_6F_{14}. A Xenon arc lamp with monochromator (resolution: 10 meV), second order filters and chopper (10 Hz) were used for excitation, and a red laser diode was used for the probe beam, whose deflection was measured by a position-sensitive quadrant photodiode via lock-in technique.

Density Functional Theory

Density functional theory (DFT) calculations were performed using the PBE functional and ultrasoft pseudo-potentials as implemented in the Quantum ESPRESSO software package.[29] All calculations were performed with kinetic energy and charge density cut-offs of 816 and 8,163 eV, respectively, with tetrahedral occupations. Initially, an optimized 24 atom super cell was prepared using an 8×8×8 k-point mesh. From this, a 3×2×3 cell was created containing 432 atoms. All subsequent calculations were carried out with a 2×2×2 k-point mesh. SCF and NSCF calculations were performed on optimized structures for defects including: hydrogen interstitial (H_{int}), oxygen vacancy (O_{vac}), bismuth vacancy (Bi_{vac}), and substitutional hydrogen for oxygen (H_O). Integrated local density of states were calculated using pp.x and visualized in VESTA.[30]
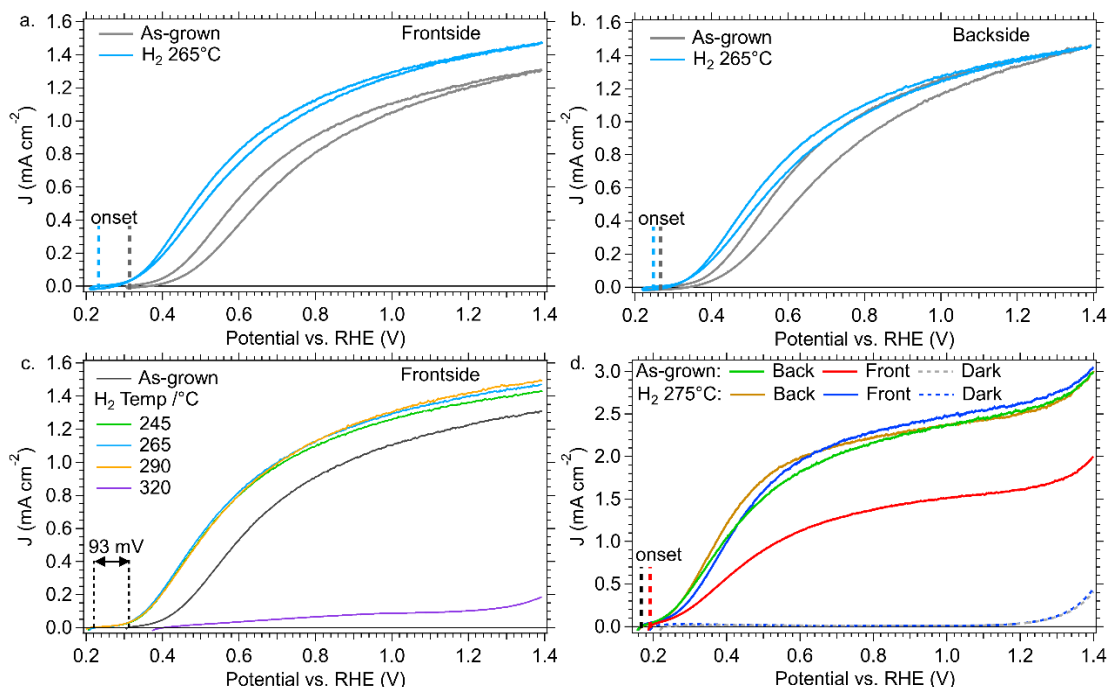
Figure 1. (a-c) Photoelectrochemical (PEC) *J-E* characteristics of spin-coated BiVO$_4$ films deposited on FTO/glass substrates and measured under AM 1.5G 1 Sun illumination in 1 M phosphate buffer (pH 6.8) with 0.1 M Na$_2$SO$_3$ as sacrificial hole acceptor. In all cases, the second cycle, scanned at 50 mV s^{-1} from the open-circuit potential to 1.4 V vs. RHE, is shown. As-deposited films are compared to films annealed in hydrogen at 265 °C under (a) frontside and (b) backside illumination. The onset potentials (*E$_{on}$*), defined as the potential at which the current density is equal to 0.001 mA cm^{-2}, are indicated with color-coded vertical dashed lines. Figure S2 compares front and backside illumination together. With no illumination, negligible currents are observed for all samples, except those annealed in H$_2$ at 320 °C, as described in the text. (c) Films annealed in H$_2$ at different temperatures are compared and *E$_{on}$* is shown for the maximum shift from the sample treated in H$_2$ at 290 °C compared to the as-grown material with frontside illumination. (d) PEC testing of nano-BiVO$_4$ samples in 0.5 M phosphate buffer with 1 M Na$_2$SO$_3$ (pH 7.16), deposited on FTO/glass substrates, showing the forward sweep of the second cycle from open-circuit voltage to 1.4 V vs. RHE. The *E$_{on}$* is shown for the H$_2$ annealed sample, which yielded the lowest value of 167 mV.

■ RESULTS AND DISCUSSION

Impact of Hydrogen Annealing on Photoelectrochemical Characteristics

Fig. 1a-b shows PEC current density vs. applied electrochemical potential (*J-E*) curves obtained from undoped, planar BiVO$_4$ photoanodes formed via spin coating. Measurements were performed under simulated AM1.5G illumination at 100 mW/cm^2 in 1 M potassium phosphate (KP$_i$) buffer at pH 6.8 containing 0.1 M SO$_3^{2-}$ as a sacrificial reagent. A summary of quantitative performance metrics for saturation current density (*J$_{sc}$*) and onset potential for photocurrent generation (*E$_{on}$*) is provided in Table 1. Significantly higher photocurrent and more negative (i.e. cathodic) onset potential are observed for the as-grown samples when illuminated from the backside (Fig. 1b) compared to the frontside (Fig. 1a). A direct comparison of these two lighting conditions is provided in Fig. S2. This difference between frontside and backside illumination has been observed previously for BiVO$_4$ photoanodes and indicates that charge carrier transport limitations in the material are associated with majority electrons rather than minority holes.[9] For the case of backside illumination, charge carriers are generated, on average, closer to the back contact and electrons have a shorter distance to travel, whereas the opposite is true for frontside illumination. The finding that electron transport limits frontside illumination performance is consistent with recent reports that electron small polarons form within the material, leading to extremely small mobilities relative to those that would be expected for band transport.[10-12]

As summarized in Table 1 and shown in Fig. 1, after annealing in hydrogen at 265 °C for 15 min, the PEC performance characteristics of spin-coated BiVO$_4$ improve significantly for frontside illumination and slightly for backside illumination. Importantly, the *J-E* characteristics for the two illumination configurations (co-plotted in Fig. S2) are nearly identical following hydrogen treatment. These results indicate that majority carrier transport limitations are largely eliminated by exposure of BiVO$_4$ to hydrogen at elevated temperature. Furthermore, *J-E* current hysteresis, which is a common feature of defect state charging, is significantly reduced with H$_2$ annealing, suggesting passivation of electronically active trap states. This is highlighted by comparing the difference between the integrated forward and reverse sweeps, Table 1.

Table 1. Photoelectrochemical (PEC) performance metrics from data shown in Fig. 1 including using both front and backside illumination: onset potential (E$_{on}$), current density at 1.23 V vs. RHE (J$_{SC}$), and the integrated charge density of the forward sweep minus the reverse sweep.

	E$_{on}$ vs. RHE (V)		J$_{SC}$ (mA cm^{-2})		Charge (C)	
Spin Coated	Front	Back	Front	Back	Front	Back
as-grown	0.31	0.27	1.24	1.38	76.5	109.7
H$_2$ 245°C	0.23	0.24	1.37	1.38	35.6	41.8
H$_2$ 265°C	0.22	0.25	1.41	1.41	40.5	47.5
H$_2$ 275°C	0.22	0.23	1.43	1.44	50	56.6
Nano-porous						
as-grown	0.19	0.17	1.63	2.56	0.11	-2.8
H$_2$ 265°C	0.18	0.17	2.53	2.64	-16.9	-8.9

The impact of the H_2 annealing temperature on PEC performance was examined by treating samples at 245, 265, 290, and 320 °C under pure H_2 at 1 atm for 15 min each. X-ray diffraction (XRD) and Raman spectroscopy confirmed that the material remained monoclinic scheelite phase $BiVO_4$ through H_2 annealing temperatures to 290 °C (see Figs. S3 & S4). Fig. 1c shows that J_{sc} increased as the H_2 annealing temperature was increased from 245 °C to 290 °C. However, at the next annealing temperature of 320 °C the sample turned visibly black and exhibited very low photocurrent. Measurement of the *J-E* curve from this sample in the dark revealed a large anodic current in the first sweep due to oxidation of metallic species that were generated by H_2-induced reduction of $BiVO_4$ (Fig. S5a), whereas H_2 treatments at lower temperature did not yield this feature. Therefore, the threshold for destructive reduction of $BiVO_4$ in 1 atm H_2 is between 290 and 320 °C, as confirmed by XRD and XPS (Figs. S3 & S5, respectively).

The results described above were obtained from undoped thin films of $BiVO_4$ deposited by spin coating. This material was selected in this study due to its excellent homogeneity, which allows reliable comparison of differently treated samples. Moreover, its low diffuse reflectance facilitates optical characterization. While the PEC performance characteristics of this material are remarkable considering that it is an undoped 50 nm thick planar film that is not optimized for light absorption (the optical absorption depth is >100 nm above the band edge), we sought to investigate the effectiveness of H_2 annealing on higher performance material. For this purpose, nanoporous $BiVO_4$ samples were prepared by the method described by Kim *et al.* on FTO-coated glass substrates.[16] The growth involves a thermally-driven reaction between aqueous electrodeposited BiOI and dropcast $VO(acac)_2$ at 450 °C for 2 h in air. Half of an individual sample (measuring 1×1 cm^2 prior to halving) was annealed in H_2 at 275 °C for 15 min. PEC measurements were performed using the same electrolyte conditions as reported by Kim *et al.* (0.5 M phosphate at pH 7.16, with 1M Na_2SO_3)[16] but larger active areas of at least 0.4 cm^2. As shown in Fig. 1d, as-grown material displayed a J_{SC} of 2.56 mA cm^{-2} with backside illumination but a significantly lower J_{SC} of 1.63 mA cm^{-2} with frontside illumination. While the H_2-annealed sample displayed similar back-illuminated performance (J_{SC} = 2.64 mA cm^{-2}), a dramatic increase of the photocurrent density was observed for frontside illumination (J_{SC} = 2.53 mA cm^{-2}). These results present an important advance for optimizing tandem cell designs in which, for example, nanoporous $BiVO_4$ would be illuminated from the frontside and monolithically integrated with a bottom cell. However, a better understanding of the underlying physical mechanisms contributing to improved PEC performance is necessary to realize its full potential and provide insight on improving the performance of next generation PEC materials.

Hydrogen Incorporation in $BiVO_4$

To determine the existence and structure of hydrogen in H_2-treated $BiVO_4$, we performed room temperature solid-state ^1H magic angle spinning (MAS) nuclear magnetic resonance (NMR) spectroscopy on as-grown and 270 °C H_2-annealed $BiVO_4$ samples. Because thin films could not be analysed using the instrumentation available, powder samples that were treated under identical conditions as thin films were used. Generally speaking, the integrated peak areas are proportional

to population density and the line width is affected by the mobility, where less mobile protons have sharper line shapes. As shown in Fig. 2, a strong signal, centered at 0.2 ppm is observed from the H_2-annealed powder. A similarly-located peak was also observed in the as-grown material, but with an amplitude that was approximately 400× lower (Fig. 2). The H_2-annealed powder exhibits additional resonances in the range of 7-9 ppm, which are not present in the as-grown material. We note that no evidence for liquid water at 4.7-4.8 ppm[31,32] was observed.

These results indicate that: (i) hydrogen is incorporated into $BiVO_4$ after annealing in H_2, (ii) at least two different chemical environments exist for the incorporated hydrogen, and (iii) hydrogen is present in the as-synthesized $BiVO_4$ in one of these chemical states. Wang and co-workers have previously calculated formation energies for hydrogen interstitials (H_{int}) and substitutional hydrogen on oxygen lattice sites (H_O), as well as for native defects, in $BiVO_4$.[23] They found that the formation energy for H_{int} is lower than for all other defects under nearly all conditions. In addition, the formation energy of H_O is low compared to native defects under the O-poor conditions encountered during H_2 annealing. Therefore, these experimental results are consistent with theoretical predictions that both hydrogen defect types are present in the material.

Based on bond and interaction distances, it is possible to predict solid-state NMR chemical shifts of different hydrogen defects in BVO_4. Hyashi *et al.* examined the ^1H chemical shifts arising from hydride (H^-) and hydroxide (OH^-) incorporated in a number of host metal oxide materials.[33] The authors discovered a linear relationship of the chemical shift with the metal-hydrogen bond distance in the hydride bond, as well as with the distance between neighbouring oxygen atoms and the hydroxide associated with interstitial hydrogen ($OH \cdots O$). Herein, density functional theory (DFT) was used to understand the structure of both hydrogen defect types and aid the assignment of the solid-state NMR resonances. For the case of H_O, geometry optimization of a hydrogen atom introduced to an oxygen vacancy reveals that the hydrogen atom becomes associated with the vanadium atom to form a HVO_3 unit with a V-H bond distance of 168 pm, which places the expected chemical shift near 0 ppm. Therefore, we conclude that the resonance observed near 0 ppm for both as-synthesized and H_2-annealed $BiVO_4$ is associated with H_O. Additionally, the sharp line shape in the H_2-annealed sample is consistent with a more localized and less mobile H associated with the defect.
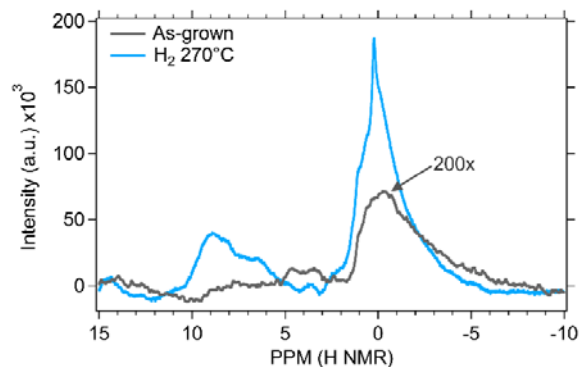
Figure 2. ^1H NMR of $BiVO_4$ powder as-grown (grey) and H_2 annealed at 270°C (blue). The signal from the as-grown sample is magnified 200× for ease of comparison. The signal at ~7-10 ppm is consistent with interstitial hydrogen and the signal at ~0 ppm is assigned to substitutional hydrogen.
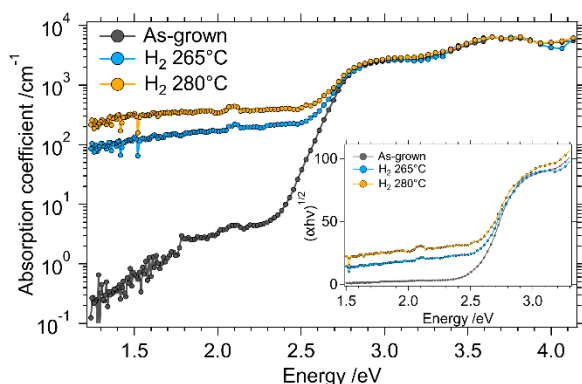
5

We note that a similar resonance has been observed in ZnO and was recently assigned to H_O in that material.[34]

For the case H_{int}, the hydrogen atom bonds to lattice oxygen to form hydroxide. A variety of structural configurations for H_{int} within $BiVO_4$ are possible and we consider one of these, as shown in (Fig. S7b and associated discussion). For this particular configuration, we find an OH⋯O distance of 265 pm, for which the expected chemical shift is 11-12 ppm.[33] While this chemical shift is larger than any of those observed experimentally, our calculation is for just one of many possible interstitial hydrogen positions in $BiVO_4$. The observed ^{1}H NMR resonance at 9 ppm is in a range that is consistent with H_{int} and suggests that their most likely positions are in locations with OH⋯O distances of 275-280 pm.[33]

From these results, it can be concluded that hydrogen incorporates into $BiVO_4$ as both H_O and H_{int} upon H_2 annealing. Importantly, our results also indicate that hydrogen is present at lower concentrations in as-grown material in the form of H_O. Although the previous prediction of defect formation energies found that H_{int} is energetically favoured,[23] it has been pointed out that H_{int} is typically highly mobile.[19,35] As such, its concentration can depend strongly on processing parameters, particularly for the case of thermal treatments.[36] Both hydrogen defect types act as donors in $BiVO_4$ and can contribute to the n-type conductivity of the material.[23] This is particularly important for synthesis of $BiVO_4$. As described above, native defect theory would predict that material synthesized under O-rich conditions, which is the typical environment used for formation of $BiVO_4$, should exhibit p-type character.[18] Our finding that hydrogen defects are present in as-synthesized $BiVO_4$ can explain the experimental observation that as-grown $BiVO_4$ is nearly always n-type.[8] The source of this hydrogen could be from decomposition of metal-organic precursors during formation and/or from water in the annealing environment, which is often laboratory air. These findings highlight that careful consideration and control over synthesis conditions is essential for achieving photoanodes with desired conductivity.

Optical and Electronic Properties of Hydrogen-Treated BiVO₄

The impact of H_2 annealing on band-edge and sub-bandgap optical absorption was studied by photothermal deflection spectroscopy (PDS), which enables quantification of the absorption coefficient with exceptional sensitivity and eliminates the influence of scattering. Fig. 3 shows a plot of the absorption coefficient (α) as a function of photon energy obtained from as-grown $BiVO_4$ on a quartz glass substrate compared to samples treated in H_2 at 265 °C and 280 °C, also on quartz. After H_2 annealing, a broad increase in the sub-bandgap absorption is observed. The inset of Fig. 3 shows Tauc plots derived from these data, which indicate an indirect bandgap of 2.5 eV for the as-grown sample, consistent with our previous report.[5] No evidence for a change of the bandgap with H_2 treatment is observed. Therefore, we can conclude that the increased photocurrent densities obtained from H_2-annealed samples do not arise from increased light harvesting associated with a reduction of the bandgap.

Although broad-spectrum sub-bandgap absorption could originate from formation of metallic clusters, neither XPS nor PEC measurements indicated their presence at H_2 annealing temperatures below 320 °C. Therefore, we consider the possibility that this absorption increase is due to d-d transitions of V^{4+} ($3d^1$), which should have transition energies in the range of $1 - 2$ eV.[6,37] It is now well established that electron small polarons in $BiVO_4$ are energetically favoured over delocalized electrons in the conduction band.[10-12] Such electron small polarons localize at V sites, leading to a change of formal oxidation state from V^{5+} ($3d^0$) to V^{4+} ($3d^1$), the concentration of which will increase with increasing electron polaron concentration. Given that H_{int} and H_O are both predicted to be donors in $BiVO_4$,[23] the concentration of V^{4+} is expected to increase with increasing hydrogen impurity concentration. Quantitative comparison of solid-state NMR performed on powders with PDS data obtained from thin films cannot be established with high accuracy. However, we note that the increase of hydrogen content in $BiVO_4$ by two orders of magnitude correlates well with the approximately two order of magnitude increase of the sub-gap optical absorption coefficient after H_2 annealing. A subgap absorption level of 100 cm⁻¹ roughly corresponds to 10^{18} cm⁻³ absorbing localized states. Considering this concentration is in good agreement with expected carrier concentrations based on previous works,[38] this suggest that optical probes, such as is presented herein, may be useful for approximating majority carrier concentrations in $BiVO_4$ due to the small polaron localization about V.

In order to detect the presence of V^{4+} states in $BiVO_4$, as shown in Fig. 4, we used electron paramagnetic resonance
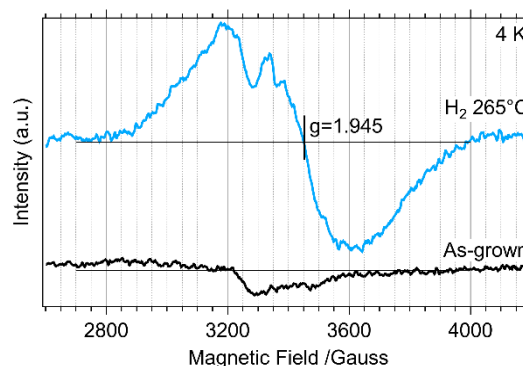

Figure 3. Absorption coefficient, measured by photothermal deflection spectroscopy, of as-grown (grey) and H_2 annealed at 265 °C (blue) and 280 °C (orange) $BiVO_4$ thin films on quartz glass substrates. Inset: Tauc plot for the indirect band gap of each film showing no significant change of the absorption onset.

Figure 4. Electron paramagnetic resonance (EPR) spectra of as-grown $BiVO_4$ (black) and 265 °C H_2 annealed $BiVO_4$ (cyan) powder samples acquired at 4 K. The EPR signal from the H_2 annealed sample is assigned to the presence of V^{4+} within the material but the lack of a well-resolved hyperfine structure indicates the simultaneous presence of multiple local environments and strong spin-spin interactions between the V^{4+} ions.

6

(EPR) spectroscopy on as-grown and H$_2$-annealed powder samples. The paramagnetic 3d^1 electronic configuration of V^{4+}, which may be present due to incorporation of defects and/or self-trapping of electrons, is characterized by electron-nuclear hyperfine splitting that arises from the magnetic interaction of the electron spin (S = ½) with the nuclear spin (I = 7/2) of ^{51}V (99.5% isotope abundance).[39-42] Thus, for an isolated electron interacting with a single ^{51}V nucleus, eight hyperfine lines should be observed. As shown in Fig. 4, we observe a broad resonance at g = 1.945, which is characteristic of V^{4+} in Bi-VO$_4$.[43] The lack of a well-defined hyperfine structure indicates strong spin-spin couplings between the V^{4+} ions within the material[41,43-46] and the simultaneous presence of structurally different V^{4+} sites arising from, for example, free polarons and defect-bound polarons associated with H$_{int}$ and H$_O$, as well as O$_{vac}$.[47] We also detect a small background EPR signal in the as-synthesized BiVO$_4$ powder samples. These results confirm that H$_2$-annealing, which increases the content of hydrogen incorporated in the material, also increases the concentration of V^{4+} sites. Previously, it was reported that increased V^{4+} content is associated with higher conductivity of BiVO$_4$ nanopowders.[44] Taken together with PEC characteristics, these observations suggest that H$_2$-annealing yields an increase of the majority carrier concentration in the form of electron small polarons, as will be discussed below.

To probe the impact of H$_2$-annealing on the Fermi level within BiVO$_4$ thin films, we performed valence band photoemission spectroscopy. Given that the binding energy is referenced to the Fermi energy (E_F), and considering the known 2.5 eV bandgap of BiVO$_4$,[5] linear fitting of the valence band edge was used to determine the Fermi level relative to the conduction band edge ($E_{CB} - E_F$) as a function of annealing condition. From this analysis, we find that E_F is located 0.61 eV below E_{CB} in the as-grown material. As shown in Fig. 5, H$_2$-annealing leads to a progressive shift of the Fermi energy towards the conduction band edge; as the annealing temperature is increased from 245 °C to 290 °C, E_F shifts from 0.49 eV to 0.44 eV below E_{CB}.

From the measured change of the Fermi level following H$_2$ annealing, it is possible to approximate the proportional increase of electron small polarons in the material. The Fermi-Dirac statistical analysis of Rettie *et al.*[12] provides the following expression for the carrier concentration, $n(T)$, in a system in which donors supply electrons to small polaron states at higher energies:

Figure 5. Valence band spectra of as-grown BiVO$_4$ (grey) and BiVO$_4$ that was H$_2$ annealed at 245 °C (green), 265 °C (blue), and 280 °C (orange). Measurements were performed on BiVO$_4$ thin films on FTO glass substrates and indicate a progressive shift of the Fermi energy towards the conduction band edge with increasing H$_2$ annealing temperature.

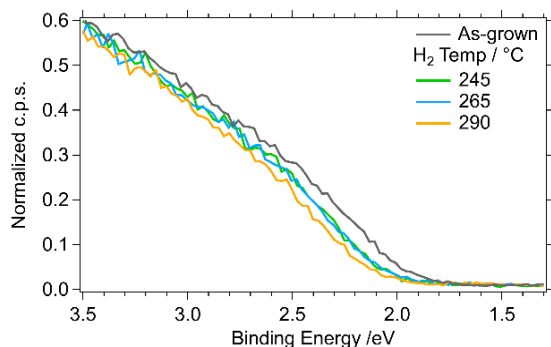$$n(T) \cong N(T)\exp(-\frac{E_m - E_F}{k_B T}) \qquad (1)$$

where $N(T)$ is the number of thermally accessible small polaron states near the energy minimum, E_m, of the small polaron band and E_F is the Fermi energy. For samples annealed in the range of 245 – 265 °C, the Fermi energy shifts by approximately 130 meV towards the conduction band edge, which corresponds to an increase of the electron small polaron concentration by a factor of approximately 150. We note that this increase of polaron concentration, derived from the change of the Fermi level position measured by photoemission spectroscopy, is in good agreement with the increased value of the sub-gap optical absorption coefficient measured by PDS of thin films.

Together, these results provide strong support for the hypothesis that hydrogen defects, in both as-grown and H$_2$ annealed samples, act as donors that affect n-type conductivity of BiVO$_4$. This conclusion is consistent with DFT calculations by Wang *et al.*, who predicted that both H$_{int}$ and H$_O$ should be donors in this material.[23] Furthermore, these findings are consistent with the model of Van de Walle,[48] in which the character of the H$_{int}$ defect is defined by the position of the Fermi level with respect to the universal hydrogen level, which is at the same energy as an electron in the standard hydrogen electrode (SHE). In the case of BiVO$_4$, for which the CBM energy is 0.1 – 0.3 eV below SHE,[6,16] interstitial hydrogen should act as a donor, as observed in our experiments. The higher carrier concentration created by H$_2$ annealing can also explain the improved PEC performance presented in Fig. 1, where increased film conductivity leads to reduced majority carrier transport limitations, as evidenced by the elimination of differences between frontside and backside illumination. Thus, increased hydrogen content plays a direct role in improving PEC characteristics.

Oxygen Vacancies in BiVO$_4$

The results presented above reveal correlations between the hydrogen content, Fermi level, sub-gap optical absorption, and PEC performance characteristics. However, it is important to recognize that H$_2$ annealing provides a reducing environment that, along with hydrogen impurity defects, could introduce oxygen vacancies into the lattice. In addition, O$_{vac}$ defects are often considered to be responsible for contributing free electron concentration and, thus, increasing the native n-type conductivity of BiVO$_4$.[17,49]

While theoretical studies predict that oxygen vacancies are shallow donor defects in BiVO$_4$,[18,49] there are, to the best of our knowledge, no experimental measurements verifying this or indicating that such states are primarily responsible for the n-type conductivity of this material. Furthermore, as discussed above, the same theory predicts that BiVO$_4$ should be p-type under the oxygen-rich synthesis conditions used for formation of thin films.[18] While the work of Vinke and co-workers[50] has been cited as indicating that O$_{vac}$ defects are responsible for the n-type conductivity of BiVO$_4$,[51] this work investigated the mixed ionic and electronic character of conductivity in BiVO$_4$ at high temperature, from 800 to 1000 K, and in the absence of illumination. This important work showed that the activation energy for electronic conduction is large relative to that of oxygen vacancy ionic conduction. Thus, they found that electronic conductivity dominates at high temperature and ionic

7

conductivity dominates at low temperature. While this study verified the n-type character of $BiVO_4$, there was no claim or experimental evidence that O_{vac} defects are responsible for electronic conduction.[50]

In order to understand the potential influence of O_{vac} on the electronic properties of as-grown and H_2 annealed material, we used DFT to calculate the densities of states (DOS) associated with this defect. Using a supercell containing 432 atoms to ensure isolation of the defects, the DOS of a single O_{vac} was calculated using PBE on the relaxed defect structures. The resulting DOS is shown in Fig. 6 and compared to the unperturbed supercell.

The bandgap of $BiVO_4$, calculated with PBE, was found to be 2.10 eV, which compares reasonably well with the experimental bandgap of 2.5 eV, considering that PBE is known to underestimate bandgaps.[5] The DOS related to O_{vac} are found deep in the gap, at 1.44 eV above the VBM. By scaling for the discrepancy in the bandgap using the scissor operator, the narrow DOS introduced by O_{vac} are predicted to lie approximately 1.7 eV above the VBM. This finding presents an apparent discrepancy with previous reports that O_{vac} defects act as shallow donors in $BiVO_4$. This was recently addressed by Kim *et al.*, whose DFT PBE+U calculations also indicated the presence of deep level states associated with O_{vac} defects in $BiVO_4$.[49] In that work, they found that the negative ionization energy of O_{vac} centers leads to spontaneous ionization to a 2+ charge state. However, it was determined that it is energetically favourable for these donated electrons to form small electron polarons via self-trapping at vanadium sites. This results in occupied electronic states deep within the $BiVO_4$ bandgap, with a binding energy of approximately 0.5 eV. Thus, while O_{vac} defects do act as donors in $BiVO_4$, they yield localized electronic states. It is important to note that interactions between negatively charged electron small polarons and positively charged oxygen vacancies could lead to bound polarons

with significantly lower mobilities than unbound polarons created by self-trapping of photogenerated charge carriers. Similar interactions between charged hydrogen defects and electron small polarons may also be present and polaron binding energies would be expected to be different for various defects. For example, it has been shown that small electron polaron binding energies to O_{vac} are considerably larger, by >400 meV, than to H_i in $BaCeO_3$.[52] In such a case, controlling conductivity of the material by introducing defects having low electron small polaron binding energies would be more effective for tuning conductivity of the semiconductor. To the best of our knowledge, polaron binding energies with different defects have not yet been studied in $BiVO_4$. However, reliable computation of such interactions, including for hydrogen defects, would be extremely valuable for advancing approaches to improving charge transport in this actively investigated photoanode material.

Although the polaron states described above should be paramagnetic, the hyperfine structure of V^{4+} measured by EPR was not well resolved and hence, it was not possible to directly establish the specific structure of the associated defect centers. Therefore, we used temperature-dependent photoluminescence (PL) spectroscopy to probe radiative recombination at deep states in $BiVO_4$. Measurements were performed on spincoated as-grown and H_2-annealed samples on quartz substrates. Consistent with our prior identification of the material as an indirect bandgap semiconductor, we find no evidence for band edge PL.[5] However, very weak sub-bandgap PL was observed at room temperature, indicating that recombination is dominated by non-radiative processes. At low temperature, a much stronger broad emission, centred at approximately 1.85 eV, was observed from both types of samples, as shown in Fig. 7. Gaussian spectral fitting indicates the presence of two components, a primary one centered at 1.86 eV and a weaker one centered between 1.60 – 1.63 eV, Fig. S8.

The temperature dependence of the PL intensity is well described by an Arrhenius behaviour with the inclusion of the T^{-2} temperature dependent capture cross section proposed by Krustok et al. and discussed in additional detail in the SI.[53] Fits generated with this model, as well as those using a double Arrhenius model, are presented in Fig. S9, with fit parameters summarized in Tables S1 & S2. The Arrhenius plot is presented in Fig. S10. Thermal quenching of the PL intensity for the as grown $BiVO_4$ film was governed by a 41 ± 2 meV activation energy. The exact origin of the thermal quenching is not yet known, but may arise from an activated competitive non-radiative recombination channel or from thermally activated delocalization of charge carriers from the defect site. We also note that the PL peak positions do not change with temperature. By comparison, the temperature dependence of the absorption spectrum is shown in Fig. S11, where the band gap of $BiVO_4$ increases with decreasing temperature. This can be modelled using phonon broadening by Eq. S4,[54] from $E_g^0 = 2.59$ eV to 2.48 eV at 350 K.

Importantly, the PL intensity is significantly reduced after H_2 annealing, by a factor of 2.6, 3.3, and 3.3 at 245 °C, 265 °C, and 290 °C, respectively. Thermal quenching of the PL intensity is also observed for H_2-treated samples, with measured activation energies in the same range, with values of 35 ± 2, 34 ± 3, and 32 ± 2 meV for the 245, 265, and 290 °C H_2-annealed samples, respectively.
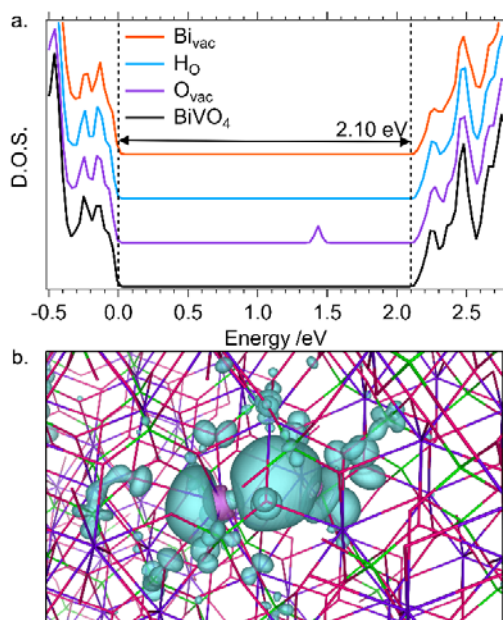
Figure 6. (a) Total density of states calculated for a 432-atom monoclinic bismuth vanadate supercell with PBE for pristine $BiVO_4$ (black) and with O_{vac} (purple), H_O (blue), and Bi_{vac} (orange) defects. (b) Integrated local density of states (ILDOS), integrated over the energy region including the mid-gap state, showing that the electronic state introduced by the O_{vac} is highly localized around the defect. Green and purple indicating regions of opposite phase.

8
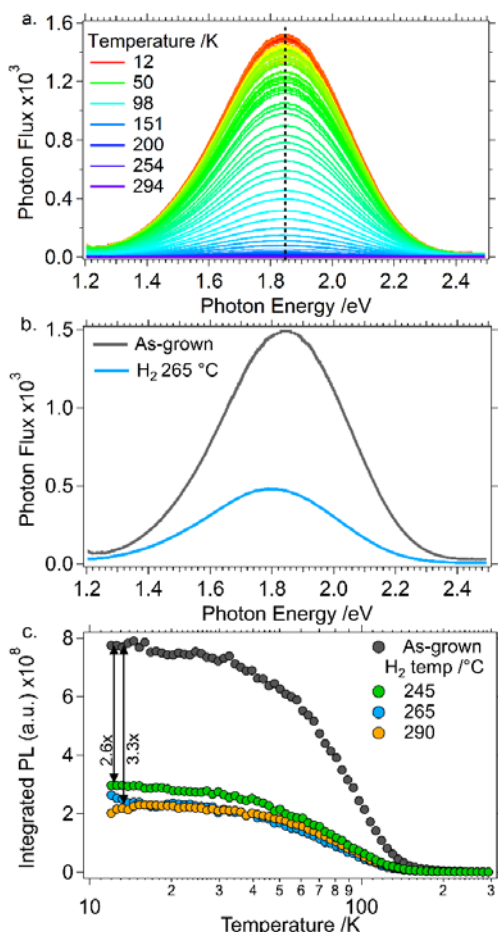
Figure 7. Photoluminescence (PL) was measured as a function of temperature on BiVO$_4$ thin films spin-coated on quartz, as-grown or annealed in H$_2$ at various temperatures and converted to photon flux vs photon energy by Equation S1. (a) PL spectra of as-grown BiVO$_4$ at a number of temperatures (red lowest, purple highest temperature). The vertical dashed line highlighting the λ_{max} shows that the photon energy is constant as a function of temperature. (b) Spectra taken at 20K are shown for as-grown (grey) and H$_2$ annealed at 265°C. Gaussian fitting of these spectra are presented in Fig. S8 which show two components at 1.86 eV and 1.60-1.63 eV. The decrease in overall PL intensity as a result of H$_2$ annealing is due to the decrease of the 1.86 eV component resulting in an apparent peak shift. The 1.6 eV feature remains unchanged after H$_2$-annealing. (c) Integrated photoluminescence intensity as a function of temperature for each annealing treatment. Annealing in H$_2$ at 245°C decreases PL intensity by a factor of 2.6, and annealing in H$_2$ at 265° or 290° decreases PL intensity by a factor of 3.3. The Ahrrenius plot is presented in SI Figure S10 and fitting is shown in SI Figure S8 and SI Tables S1 & S2.

The PL emission energy corresponds very well with the calculated deep level electronic states arising from O$_{vac}$ defects at low temperature. However, quenching of this emission with H$_2$ annealing would suggest a reduction, rather than an increase, of the O$_{vac}$ concentration under these reducing treatments. In order to determine if other midgap states within BiVO$_4$ could be responsible for the observed emission, the DOS of Bi$_{vac}$ was also calculated using DFT. Yin *et al.* studied a variety of intrinsic defects and extrinsic dopants in BiVO$_4$ by GGA and found lowest formation energies for Bi$_{vac}$ (acceptor) and O$_{vac}$ (donor), with equilibrium between the two defining Fermi level pinning energies in different synthesis environments.[18] However, as shown in Fig. 6a, no deep level DOS are introduced into the bandgap of BiVO$_4$ due to Bi$_{vac}$. Therefore, we conclude that the most likely origin of the observed PL in BiVO$_4$ is associated with recombination of electron small polarons bound to oxygen vacancy defect centers with photoexcited holes. We note that luminescent oxygen vacancies have

also been observed and calculated in other metal oxides, such as SrTiO$_3$, in which the level is present at 0.4 eV below the CB edge.[55-57]

As described above, solid-state NMR indicates a significant increase in the concentration of substitutional H$_O$ following H$_2$ annealing. Therefore, we also apply DFT to determine the effect of incorporating a hydrogen atom onto an oxygen vacancy center. As shown in Fig. 6a, the DOS arising from O$_{vac}$, which is located deep within the bandgap, is eliminated by hydrogen. This finding is consistent with the observed reduction of PL intensity from BiVO$_4$ upon H$_2$ annealing.

The magnitude of PL reduction is not commensurate with the observed increase of hydrogen content in the films, the carrier concentration needed for the measured change in the Fermi level, or the increase in sub-gap optical absorption. This suggests that substitutional hydrogen is not solely incorporated at oxygen vacancy sites that were already present in as-grown material. Rather, these results are consistent with the conclusion that H$_2$ annealing does result in a decrease of the total oxygen content within the bulk of the material but, at the same time, hydrogen is substitutionally incorporated at these sites, leading to preferential formation of H$_O$ rather than O$_{vac}$.

■ **CONCLUSION**

Post-synthetic processing of BiVO$_4$ photoanodes by H$_2$ annealing was found to enhance its PEC performance characteristics under AM 1.5G simulated solar illumination, yielding improved onset potential for photoanodic current, increased fill factor of *J-E* curves, and near-complete elimination of majority carrier charge transport limitations. To understand the role of hydrogen annealing on the functional characteristics of BiVO$_4$, we employed a variety of spectroscopic methods that, together, revealed that hydrogen is incorporated in the material at both interstitial (H$_{int}$) and substitutional (H$_O$) sites. The result was a shift of the Fermi level towards the conduction band that, considered alongside recent transport measurements in BiVO$_4$,[9-12] indicated a higher concentration of electron small polarons. Temperature-dependent photoluminescence measurements showed that H$_2$ annealing reduced radiative recombination at deep trap states associated with oxygen vacancy (O$_{vac}$) defects in the as-grown material. Thus, while annealing of BiVO$_4$ in hydrogen can reduce the oxygen content in the material, the primary effect is not due to introduction of oxygen vacancies but, rather, incorporation of hydrogen donors into the material. As a consequence, the photoelectrochemical performance characteristics are significantly improved under frontside illumination conditions due to reduced majority carrier transport limitations.

The results presented here indicate that hydrogen acts as a donor in BiVO$_4$ and its presence in as-grown material provides a resolution to the discrepancy between experiment and theory on the native conductivity of material synthesized under oxygen rich conditions; electronically active hydrogen defects incorporated during synthesis can play a defining role in the n-type character of this promising photoanode material. This work highlights that addressing the role of native and impurity defects, methods of passivating deep level states, and the active role of hydrogen in BiVO$_4$ and other metal oxide semiconductor systems is critical for understanding and controlling functional performance. Furthermore, these findings have important implications on electron small polaron transport in

9

BiVO$_4$, which has recently been discovered to dominate over band transport. Small electron polaron binding energies at different impurity and defect sites are expected to have a significant impact on the ability to affect conductivity of the material. Our measurements, which indicate that hydrogen impurities act as effective donors in BiVO$_4$ and play a defining role in the achieved conductivity of as-grown material, suggest a pressing need for detailed theoretical assessment of polaron-defect interactions in BiVO$_4$.

■ ASSOCIATED CONTENT

Supporting Information
The Supporting Information is available free of charge on the ACS Publications website at DOI:.

■ AUTHOR INFORMATION

Corresponding Author
 *E-mail: idsharp@lbl.gov
Notes
The authors declare no competing financial interest.

■ ACKNOWLEDGMENTS

■ REFERENCES

(1) Lewis, N. S.; Nocera, D. G. Powering the Planet: Chemical Challenges in Solar Energy Utilization *Proc. Natl. Acad. Sci. U. S. A.* **2006**, *103*, 15729-15735.

(2) Krol, R. v. d.; Grätzel, M. *Photoelectrochemical Hydrogen Production*; Springer: New York, 2012.

(3) Bard, A. J.; Faulkner, L. R. *Electrochemical Methods: Fundamentals and Applications*; 2nd ed.; Wiley: New York, 2001.

(4) Smith, W. A.; Sharp, I. D.; Strandwitz, N. C.; Bisquert, J. Interfacial Band-Edge Energetics for Solar Fuels Production *Energy Environ. Sci.* **2015**, *8*, 2851-2862.

(5) Cooper, J. K.; Gul, S.; Toma, F. M.; Chen, L.; Liu, Y.-S.; Guo, J.; Ager, J. W.; Yano, J.; Sharp, I. D. Indirect Bandgap and Optical Properties of Monoclinic Bismuth Vanadate *J. Phys. Chem. C* **2015**, *119*, 2969-2974.

(6) Cooper, J. K.; Gul, S.; Toma, F. M.; Chen, L.; Glans, P.-A.; Guo, J.; Ager, J. W.; Yano, J.; Sharp, I. D. Electronic Structure of Monoclinic BiVO4 *Chem. Mater.* **2014**, *26*, 5365-5373.

(7) Hu, S.; Xiang, C. X.; Haussener, S.; Berger, A. D.; Lewis, N. S. An Analysis of the Optimal Band Gaps of Light Absorbers in Integrated Tandem Photoelectrochemical Water-Splitting Systems *Energy Environ. Sci.* **2013**, *6*, 2984-2993.

(8) Park, Y.; McDonald, K. J.; Choi, K. S. Progress in Bismuth Vanadate Photoanodes For Use In Solar Water Oxidation *Chem. Soc. Rev.* **2013**, *42*, 2321-2337.

(9) Abdi, F.; van de Krol, R. Nature and Light Dependence of Bulk Recombination in Co-Pi-Catalyzed BiVO4 Photoanodes *J. Phys. Chem. C* **2012**, *116*, 9398-9404.

(10) Rettie, A. J. E.; Lee, H. C.; Marshall, L. G.; Lin, J. F.; Capan, C.; Lindemuth, J.; McCloy, J. S.; Zhou, J.; Bard, A. J.; Mullins, C. B. Combined Charge Carrier Transport and Photoelectrochemical Characterization of BiVO4 Single Crystals: Intrinsic Behavior of a Complex Metal Oxide *J. Am. Chem. Soc.* **2013**, *135*, 11389-11396.

(11) Rettie, A. J. E.; Chemelewski, W. D.; Lindemuth, J.; McCloy, J. S.; Marshall, L. G.; Zhou, J.; Emin, D.; Mullins, C. B. Anisotropic Small-Polaron Hopping in W:BiVO4 Single Crystals *Appl. Phys. Lett.* **2015**, *106*, 022106.

(12) Rettie, A. J. E.; Chemelewski, W. D.; Emin, D.; Mullins, C. B. Unravelling Small-Polaron Transport in Metal Oxide Photoelectrodes *J. Phys. Chem. Lett.* **2016**, *7*, 471-479.

(13) Abdi, F. F.; Han, L. H.; Smets, A. H. M.; Zeman, M.; Dam, B.; van de Krol, R. Efficient Solar Water Splitting by Enhanced Charge Separation in a Bismuth Vanadate-Silicon Tandem Photoelectrode *Nat. Commun.* **2013**, *4*, 1-7.

(14) Shi, X.; Choi, I. Y.; Zhang, K.; Kwon, J.; Kim, D. Y.; Lee, J. K.; Oh, S. H.; Kim, J. K.; Park, J. H. Efficient Photoelectrochemical Hydrogen Production From Bismuth Vanadate-Decorated Tungsten Trioxide Helix Nanostructures *Nat. Commun.* **2014**, *5*, 1-8.

(15) Chen, L.; Toma, F. M.; Cooper, J. K.; Lyon, A.; Lin, Y.; Sharp, I. D.; Ager, J. W. Mo-Doped BiVO4 Photoanodes Synthesized by Reactive Sputtering *ChemSusChem* **2015**, *8*, 1066-1071.

(16) Kim, T. W.; Choi, K. S. Nanoporous BiVO4 Photoanodes with Dual-Layer Oxygen Evolution Catalysts for Solar Water Splitting *Science* **2014**, *343*, 990-994.

(17) Liang, Y.; Tsubota, T.; Mooij, L. P. A.; van de Krol, R. Highly Improved Quantum Efficiencies for Thin Film BiVO4 Photoanodes *J. Phys. Chem. C* **2011**, *115*, 17594-17598.

(18) Yin, W. J.; Wei, S. H.; Al-Jassim, M. M.; Turner, J.; Yan, Y. Doping Properties of Monoclinic BiVO4 Studied by First-Principles Density-Functional Theory *Phys. Rev. B: Condens. Matter Mater. Phys.* **2011**, *83*, 155102/155101-155102/155111.

(19) Walle, C. G. V. d.; Neugebauer, J. Hydrogen In Semiconductors *Annu. Rev. Mater. Res.* **2006**, *36*, 179-198.

(20) Meyer, B.; Alves, H.; Hofmann, D.; Kriegseis, W.; Forster, D.; Bertram, F.; Christen, J.; Hoffmann, A.; Straßburg, M.; Dworzak, M. Bound Exciton and Donor–Acceptor Pair Recombinations in ZnO *Phys. Status Solidi B* **2004**, *241*, 231-260.

(21) Van de Walle, C. G. Hydrogen as a Cause of Doping in Zinc Oxide *Phys. Rev. Lett.* **2000**, *85*, 1012-1015.

(22) Gan, J.; Lu, X.; Rajeeva, B. B.; Menz, R.; Tong, Y.; Zheng, Y. Efficient Photoelectrochemical Water Oxidation over Hydrogen-Reduced Nanoporous BiVO4 with Ni–Bi Electrocatalyst *ChemElectroChem* **2015**, *2*, 1385-1395.

(23) Wang, G.; Ling, Y.; Lu, X.; Qian, F.; Tong, Y.; Zhang, J. Z.; Lordi, V.; Rocha Leao, C.; Li, Y. Computational and Photoelectrochemical Study of Hydrogenated Bismuth Vanadate *J. Phys. Chem. C* **2013**, *117*, 10957-10964.

(24) Singh, A. P.; Kodan, N.; Dey, A.; Krishnamurthy, S.; Mehta, B. R. Improvement in the Structural, Optical, Electronic and

10

Photoelectrochemical Properties of Hydrogen Treated Bismuth Vanadate Thin Films *Int. J. Hydrogen Energy* **2015**, *40*, 4311-4319.

(25) Jeon, T. H.; Choi, W.; Park, H. Cobalt-phosphate complexes catalyze the photoelectrochemical water oxidation of BiVO4 electrodes *Phys. Chem. Chem. Phys.* **2011**, *13*, 21392-21401.

(26) Lichterman, M. F.; Shaner, M. R.; Handler, S. G.; Brunschwig, B. S.; Gray, H. B.; Lewis, N. S.; Spurgeon, J. M. Enhanced Stability and Activity for Water Oxidation in Alkaline Media with Bismuth Vanadate Photoelectrodes Modified with a Cobalt Oxide Catalytic Layer Produced by Atomic Layer Deposition *J. Phys. Chem. Lett.* **2013**, *4*, 4188-4191.

(27) Seabold, J. A.; Choi, K.-S. Efficient and Stable Photo-Oxidation of Water by a Bismuth Vanadate Photoanode Coupled with an Iron Oxyhydroxide Oxygen Evolution Catalyst *J. Am. Chem. Soc.* **2012**, *134*, 2186-2192.

(28) Ambacher, O.; Rieger, W.; Ansmann, P.; Angerer, H.; Moustakas, T. D.; Stutzmann, M. Sub-Bandgap Absorption of Gallium Nitride Determined by Photothermal Deflection Spectroscopy *Solid State Commun.* **1996**, *97*, 365-370.

(29) Giannozzi, P.; Baroni, S.; Bonini, N.; Calandra, M.; Car, R.; Cavazzoni, C.; Ceresoli, D.; Chiarotti, G. L.; Cococcioni, M.; Dabo, I.; Dal Corso, A.; Fabris, S.; Fratesi, G.; de Gironcoli, L.; Gebauer, R.; Gerstmann, U.; Gougoussis, C.; Kokalj, A.; Lazzeri, M.; Martin-Samos, L.; Marzari, N.; Mauri, F.; Mazzarello, R.; Paolini, S.; Pasquarello, A.; Paulatto, L.; Sbraccia, C.; Scandolo, S.; Sclauzero, G.; Seitsonen, A. P.; Smogunov, A.; Umari, P.; Wentzcovitch, R. M. QUANTUM ESPRESSO: A Modular and Open-Source Software Project for Quantum Simulations of Materials *J. Phys.: Condens. Matter* **2009**, *21*, 395502.

(30) Momma, K.; Izumi, F. VESTA 3 For Three-Dimensional Visualization of Crystal, Volumetric and Morphology Data *J. Appl. Crystallogr.* **2011**, *44*, 1272-1276.

(31) Ladizhansky, V.; Hodes, G.; Vega, S. Solid State NMR Study of Water Binding on the Surface of CdS Nanoparticles *J. Phys. Chem. B* **2000**, *104*, 1939-1943.

(32) Nosaka, A. Y.; Fujiwara, T.; Yagi, H.; Akutsu, H.; Nosaka, Y. Characteristics of Water Adsorbed on TiO2 Photocatalytic Systems with Increasing Temperature as Studied by Solid-State 1H NMR Spectroscopy *J. Phys. Chem. B* **2004**, *108*, 9121-9125.

(33) Hayashi, K.; Sushko, P. V.; Hashimoto, Y.; Shluger, A. L.; Hosono, H. Hydride Ions in Oxide Hosts Hidden by Hydroxide Ions *Nat Commun* **2014**, *5*.

(34) Wang, M.; Yu, G.; Ji, W.; Li, L.; Ding, W.; Peng, L. Identification of Intrinsic Hydrogen Impurities in ZnO With 1H Solid-State Nuclear Magnetic Resonance Spectroscopy *Chem. Phys. Lett.* **2015**, *627*, 7-12.

(35) Janotti, A.; Varley, J. B.; Lyons, J. L.; Walle, C. G. In *Functional Metal Oxide Nanostructures*; Wu, J., Cao, J., Han, W.-Q., Janotti, A., Kim, H.-C., Eds.; Springer New York: New York, NY, 2012, p 23-35.

(36) Janotti, A.; Van de Walle, C. G. Hydrogen Multicentre Bonds *Nat. Mater.* **2007**, *6*, 44-47.

(37) Benmoussa, M.; Ibnouelghazi, E.; Bennouna, A.; Ameziane, E. L. Structural, Electrical and Optical Properties of Sputtered Vanadium Pentoxide Thin Films *Thin Solid Films* **1995**, *265*, 22-28.

(38) Abdi, F. F.; Savenije, T. J.; May, M. M.; Dam, B.; van de Krol, R. The Origin of Slow Carrier Transport in BiVO4 Thin Film Photoanodes: A Time-Resolved Microwave Conductivity Study *J. Phys. Chem. Lett.* **2013**, *4*, 2752-2757.

(39) Yasoda, B.; Sreekanth Chakradhar, R. P.; Rao, J. L.; Gopal, N. O. EPR and Optical Absorption Studies of VO^{2+} Ions in Alkaline Earth Aluminoborate Glasses *Mater. Chem. Phys.* **2007**, *106*, 33-38.

(40) Alvarez, G. Electron Paramagnetic Resonance of Transition Metal Ions in Glasses: Recent Progresses *ChemInform* **2012**, *43*, 181-202.

(41) Kerkouri, N.; Haddad, M.; Et-tabirou, M.; Chahine, A.; Laânab, L. FTIR, Raman, EPR and Optical Absorption Spectral Studies on V$_2$O$_5$-Doped Cadmium Phosphate Glasses *Physica B: Condensed Matter* **2011**, *406*, 3142-3148.

(42) Seth, V. P.; Gupta, S.; Jindal, A.; Gupta, S. K. ESR of Vanadyl Ions in Li$_2$O · BaO · B$_2$O$_3$ Glasses *J. Non-Cryst. Solids* **1993**, *162*, 263-267.

(43) Shantha, K.; Varma, K. B. R. Preparation and Characterization of Nanocrystalline Powders of Bismuth Vanadate *Mater. Sci. Eng., B* **1999**, *60*, 66-75.

(44) Venkatesan, R.; Velumani, S.; Tabellout, M.; Errien, N.; Kassiba, A. Dielectric Behavior, Conduction and EPR Active Centres in BiVO4 Nanoparticles *J. Phys. Chem. Solids* **2013**, *74*, 1695-1702.

(45) Vedeanu, N.; Stanescu, R.; Filip, S.; Ardelean, I.; Cozar, O. IR and ESR Investigations on V$_2$O$_5$–P$_2$O$_5$–BaO Glass System With Opto-Electronic Potential *J. Non-Cryst. Solids* **2012**, *358*, 1881-1885.

(46) Stefan, R.; Simedru, D.; Popa, A.; Ardelean, I. Structural Investigations of V$_2$O$_5$–P$_2$O$_5$–CaO Glass System by FT-IR and EPR Spectroscopies *J. Mater. Sci.* **2012**, *47*, 3746-3751.

(47) Tinet, D.; Legay, M. H.; Gatineau, L.; Fripiat, J. J. Properties of the Vanadium Pentoxide Hydrogen Bronzes (H$_{2x}$V$_2$O$_5$) *J. Phys. Chem.* **1986**, *90*, 948-952.

(48) Van de Walle, C. G.; Neugebauer, J. Universal Alignment of Hydrogen Levels in Semiconductors, Insulators and Solutions *Nature* **2003**, *423*, 626-628.

(49) Kim, T. W.; Ping, Y.; Galli, G. A.; Choi, K.-S. Simultaneous Enhancements in Photon Absorption and Charge Transport of Bismuth Vanadate Photoanodes for Solar Water Splitting *Nat. Commun.* **2015**, *6*.

(50) Vinke, I. C.; Diepgrond, J.; Boukamp, B. A.; de Vries, K. J.; Burggraaf, A. J. Bulk and Electrochemical Properties of BiVO4 *Solid State Ionics* **1992**, *57*, 83-89.

(51) Long; Cai; Kisch, H. Visible Light Induced Photoelectrochemical Properties of n-BiVO$_4$ and n-BiVO$_4$/p-Co$_3$O$_4$ *J. Phys. Chem. C* **2008**, *112*, 548-554.

(52) Swift, M.; Janotti, A.; Van de Walle, C. G. Small Polarons and Point Defects in Barium Cerate *Phys. Rev. B* **2015**, *92*, 214114.

(53) Krustok, J.; Collan, H.; Hjelt, K. Does the Low-Temperature Arrhenius Plot of the Photoluminescence Intensity in CdTe Point Towards an Erroneous Activation Energy? *J. Appl. Phys.* **1997**, *81*, 1442-1445.

(54) O'Donnell, K. P.; Chen, X. Temperature Dependence of Semiconductor Band Gaps *Appl. Phys. Lett.* **1991**, *58*, 2924-2926.

(55) Janotti, A.; Varley, J. B.; Choi, M.; Van de Walle, C. G. Vacancies and Small Polarons in SrTiO$_3$ *Phys. Rev. B* **2014**, *90*, 085202.

(56) Yamada, Y.; Yasuda, H.; Tayagaki, T.; Kanemitsu, Y. Temperature Dependence of Photoluminescence Spectra of Nondoped and Electron-Doped SrTiO$_3$: Crossover from Auger Recombination to Single-Carrier Trapping *Phys. Rev. Lett.* **2009**, *102*, 247401.

(57) Hasegawa, T.; Shirai, M.; Tanaka, K. Localizing Nature of Photo-Excited States in SrTiO$_3$ *J. Lumin.* **2000**, *87–89*, 1217-1219.

11

TOC Graphic

H-defects in BiVO$_4$:
Doping and Passivation